Scientific paper

Radiation-induced alteration of meta-chert[1]

Ippei Maruyama[1*,2], Toshiaki Kondo [3], Shohei Sawada[4], Patricie Halodova[5], Alica Fedorikova[6], Takahiro Ohkubo [7], Kenta Murakami [8], Takafumi Igari[9], Elena Tajuelo Rodriguez[10], Kiyoteru Suzuki [11]

[1] Professor, Graduate School of Engineering, The University of Tokyo, Tokyo, Japan.
[*]Corresponding author, *E-mail:* i.maruyama@bme.arch.t.u-tokyo.ac.jp

[2] Professor, Graduate School of Environmental Studies, Nagoya University, Nagoya, Japan.

[3] Engineer, Nuclear Power Department, Kajima Corporation, Tokyo, Japan.

[4] Group Leader, Nuclear Power Department, Kajima Corporation, Tokyo, Japan.

[5] Group leader, Department of Material Analysis, Centrum výzkumu Řež s.r.o, Czech Republic

[6] Group leader, Department of Material Analysis, Centrum výzkumu Řež s.r.o, Czech Republic

[7] Assoc. Prof., Graduate School of Engineering, Chiba University, Chiba, Japan, Japanese.

[8] Assoc. Prof., Graduate School of Engineering, The University of Tokyo, Toyo, Japan.

[9] Manager, Technology Safety Department, MRI Research Associates Inc., Japan.

[10] R&D Staff Member, Nuclear Structures and Construction Group, Oak Ridge National Laboratory, USA.

[11] Research Director, Societal Safety and Industrial Innovation Division, Mitsubishi Research Institute, Inc., Tokyo, Japan.

Abstract

Concrete aggregate identified as "meta-chert" was irradiated with gamma-rays and neutrons. To identify the volume expansion of the aggregate under neutron irradiation, the following analyses were performed for pristine and irradiated α-quartz and meta-chert: X-ray diffraction (XRD)/Rietveld analysis, dimension change, water pycnometry, He-pycnometry, light optical microscopy (LOM), and scanning electron microscopy (SEM). From the difference of volume expansion observed from dimension change and water / helium pycnometry, the crack opening inside the aggregate subjected to irradiation was elucidated, and this was confirmed by LOM and SEM analysis. The crack contribution to the expansion of the aggregate was significant for neutron fluence > 6.99×10^{19} n/cm^2, for E $\geqq$ 0.01 MeV. Based on the XRD analysis, changes

[1] This manuscript has been co-authored by UT-Battelle, LLC, under contract DE-AC05-00OR22725 with the US Department of Energy (DOE). The publisher acknowledges the US government license to provide public access under the DOE Public Access Plan (hxxp://energy.gov/downloads/doe-public-access-plan).

in lattice parameters were identified and the cell volume expansion was compared with the data by helium pycnometry. Based on the density change calculation and phase calculation data, the density of X-ray amorphous phase was consistent with that of expanded crystal quartz.

Keywords: Neutron irradiation, rock-forming minerals, amorphization, metamictication, volume expansion

1. Introduction

Electricity from nuclear power plants is an essential base-load power source. In this regard, the long-term operation of nuclear power plants is an issue to be addressed. From the perspective of concrete engineering, it is necessary to study the integrity of concrete structural members in environments exposed to neutron and gamma-ray irradiation . However, there is little data and experience available to evaluate this aspect. The deterioration of concrete owing to neutrons is caused by the radiation-induced volumetric expansion (RIVE) of the constituent aggregate (Elleuch et al., 1972; Hilsdorf et al., 1978; Maruyama et al., 2017b). To establish a process for evaluating concrete degradation as a function of time, several research gaps ought to be considered. The following points can offer an effective pathway to address the research gaps:

1) Investigation of the RIVE of rock-forming minerals as a function of neutron fluence, neutron flux, and temperature (Simon, 1957; Primak, 1958; Bates et al., 1974; Bykov et al., 1981; Douillard and Duraud, 1996; Yuan et al., 2001; Mota et al., 2005; Denisov et al., 2012; Wang et al., 2015; Hsiao et al., 2017; Krishnan et al., 2017a, 2017b; Silva et al., 2018; Le Pape et al., 2020; Okada et al., 2020; Silva et al., 2022);
2) Investigation of aggregate expansion considering the inhomogeneous volume expansion of rock-forming minerals (Elleuch et al., 1972; Hilsdorf et al., 1978; Denisov et al., 2012; Maruyama et al., 2017b; Khmurovska and Štemberk, 2021a, 2021b),
3) Deriving concrete degradation as a function of aggregate expansion (Dubrovskii et al., 1966b, 1966a, 1968, 1970; Elleuch et al., 1972; Hilsdorf et al., 1978; Denisov et al., 2012; Giorla et al., 2015; Le Pape et al., 2015, 2016; Pomaro, 2016; Maruyama et al., 2017b; Li et al., 2020; Sasano et al., 2020; Saklani et al., 2021; Torrence et al., 2021; Pomaro et al., 2022);
4) Performance evaluation of reinforced concrete members considering neutron attenuation and resultant distribution of degradation under complex restraint conditions (Bruck et al., 2019; Kambayashi et al., 2020).

To the best of the authors' knowledge, the data on the damage in aggregate experiencing radiation-induced volumetric expansion of rock-forming minerals are extremely limited, and no appropriate data are available to validate numerical models that can identify the scale differences between rock-forming minerals and volume expansion of aggregates. The most neutron-sensitive rock-forming mineral is α-quartz (Wittels and Sherrill, 1954; Primak, 1958; Denisov et al., 2012; Field et al., 2015; Ichikawa et al., 2017; Le Pape et al., 2018). Considering this background, meta-chert, comprising α-quartz as the major mineral composition, was investigated as the simplest aggregate.

2. Materials and methods

2.1 Materials

Meta-chert was used in this study. This aggregate was termed as thermally altered tuff in a

previous study (Maruyama et al., 2017b). As this specimen contains more than 90 % by mass of α-quartz, we re-categorized it as meta-chert. Meta-chert was developed from boulders of approximately 30 cm diameter, which were collected from Aichi prefecture in Japan. X-ray powder diffraction (XRD) measurements were performed to select samples with similar phase contents for the experiments. Typical XRD/Rietveld analysis results are shown in Table 1, and the typical X-ray fluorescence-based oxide composition and loss of ignition (LOI) are shown in Table 2.

Table 1 Mineral composition (Maruyama et al., 2017b)

	Mass %	1σ
Quartz	91.86337	1.917816
Albite	0.76761	0.211093
Anorthite	2.29323	0.573308
Anorthoclase	0.61313	0.402367
Orthoclase	0.50374	0.406867
Microcline	3.02245	0.631271
Biotite	0.44233	0.068935
Chlorite	0.50374	0.271245
Total	100.0096	

Table 2 Chemical composition (Maruyama et al., 2017b)

LOI (%)		0.93
Oxides Composition	SiO_2	86.99
	Al_2O_3	5.09
	Fe_2O_3	2.25
	CaO	0.68
	MgO	0.98
	SO_3	0.69
	Na_2O	0.49
	K_2O	1.25
	TiO_2	0.24
	P_2O_5	0.1
	MnO	0.17
	Total	99.86

2.2 Irradiation

(1) Gamma-ray irradiation

A gamma-ray irradiation experiment was conducted at the Cobalt-60 irradiation facility of the

Takasaki Advanced Radiation Research Institute, Japan. The specimens were irradiated with three different absorption doses: 27 MGy, 55 MGy, and 108 MGy. The average gamma-ray dose rates were 11.15 kGy/h, 10.92 kGy/h, and 10.89 kGy/h, respectively, which were confirmed using alanine dosimeters. The specimen size was $\phi 45 \times 90$ mm^3, and five specimens were used for each condition. A companion heating experiment was conducted for two purposes: (1) to reproduce the temperature history of the specimens to separate the gamma-ray irradiation impact from the gamma-ray heating, and (2) to confirm the property change of the specimen immediately after the sudden temperature change from room temperature to 65 ℃. During the gamma-ray irradiation, the temperature changes were in the range of 10–50 ℃. More information regarding the temperature monitoring can be found in Section 2.3.

(2) Neutron irradiation

A neutron irradiation experiment was conducted in the JEEP-II reactor in Norway. This research reactor was selected because of the heavy water reaction, which yields a lower gamma-ray dose and the resultant gamma heating energy was lower than that of a light water reactor. The reactor hole positions 36 and 52, which provided approximately identical irradiation conditions, were used. The neutron fluences were measured using monitoring wires, and the neutron fluence of each specimen was calibrated using the MCNP model (Brown et al., 2002). The evaluated neutron fluences of the four capsules are summarized in Table 3. These data were adopted from a previous report (Maruyama et al., 2017b), focusing on aggregate specimens.

During the irradiation, thermal calculations suggested that the temperature of the specimens was approximately 53.3 ℃ and there was a small temperature gradient within the specimens. A previous study has provided detailed temperature information (Maruyama et al., 2017b).

The specimen size was $\phi 10 \times 10$ mm^3, and six meta-chert specimens were irradiated for each neutron fluence. Seven concrete specimens with dimensions of $\phi 40 \times 60$ mm^3, 30 different aggregate specimens, and six hardened cement paste specimens with the same dimensions were irradiated. Details of the irradiation conditions, capsule design, and monitoring data were adopted from a previous study (Maruyama et al., 2017b).

Table 3 Irradiation conditions for the specimens

Capsule	Neutron fluence (n/cm^2)			Neutron fluence (1σ)			Gamma-ray	
	≧1 MeV	≧ 0.1 MeV	≧ 0.01 MeV	≧1 MeV	≧ 0.1 MeV	≧ 0.01 MeV	Flux (kGy/h)	Dose (kGy)
PPT-B	2.94E+18 ~2.80E+18	7.77E+18 ~7.45E+18	1.24E+19 ~1.18E+19	3.49E+16 ~3.41E+16	5.70E+16 ~5.58E+16	7.17E+16 ~7.01E+16	1.83E+02 ~1.68E+02	1.11E+05 ~1.01E+05
PPT-C	5.50E+18 ~5.17E+18	1.41E+19 ~1.35E+19	2.21E+19 ~2.13E+19	6.91E+16 ~6.70E+16	1.11E+17 ~1.09E+17	1.39E+17 ~1.35E+17	1.86E+02 ~1.75E+02	2.02E+05 ~1.90E+05
PPT-D	1.76E+19 ~1.65E+19	4.55E+19 ~4.33E+19	7.13E+19 ~6.83E+19	2.22E+17 ~2.16E+17	3.59E+17 ~3.49E+17	4.48E+17 ~4.37E+17	1.72E+02 ~1.62E+02	6.42E+05 ~6.07E+05
PPT-E	4.14E+19 ~3.29E+19	9.87E+19 ~8.67E+19	1.51E+20 ~1.38E+20	5.43E+17 ~3.98E+17	7.71E+17 ~6.52E+17	9.17E+17 ~8.18E+17	1.81E+02 ~1.68E+02	1.30E+06 ~1.21E+06

2.3 Measurement

(1) Temperature

Thermocouples were attached to the surface of the specimens during gamma-ray irradiation for temperature measurements. One thermocouple was attached to the surface nearest to the gamma-ray irradiation source and another was attached to the opposite surface. The obtained data were used to control the temperature of the specimens during the dummy heating experiments.

(2) Compressive strength

Compressive loading was conducted on the specimens before and after gamma-ray irradiation according to JIS A 1108:2006. The compressive strength and Young's modulus of the specimens were determined based on a loading experiment (Maekawashikenki, ACA-100A-B2, 200 kN maximum).

(3) Mass change

The masses of the gamma-ray irradiated specimens were recorded before and after irradiation (or heating) using a precision balance (Shimazu, BL-620S) with an accuracy of 0.01 g. The mass change in the specimens for neutron irradiation was recorded using a precision balance with an accuracy of 0.001 g (VWR, LPW-723i).

(4) Dimension change

The change in the dimensions of the gamma-irradiated specimen was measured using a micrometer caliper with a resolution of 0.01 mm. Five different locations were used for the diameter change, and two other locations were used for the length change. For neutron irradiation, a micrometer with a resolution of 0.001 mm was used for measurement. Three different sets of positions on both end surfaces were used to measure the length of the specimen, and five other groups of positions on the side surface were used for the diameter (Figure 1 displays five different diameters). The averaged value was used for each position.

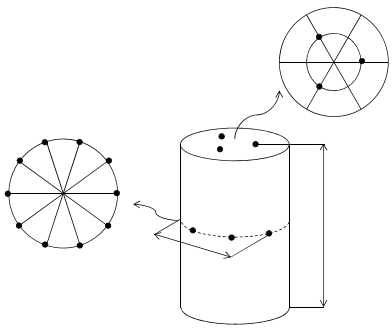

Fig. 1 Schematic figure of locations for dimension measurement of aggregate specimens (Maruyama et al., 2017)

(5) X-ray powder diffraction

After the compressive strength experiment of the gamma-ray-irradiated specimens, the pieces were crushed and ground in an agate mortar to a fine powder, such that it could not be felt on the fingertips. X-ray diffraction patterns were obtained using an X'Pert RPD MPD

(PANalytical) with a conventional X-ray tube (Cu-Kα, λ = 1.542 Å, 45 kV, 40 mA, line focus) operated in reflection mode, with a Soller slit of 1 °, divergence slit of 2 °, receiving slit of 5.5 mm, scanning range of 2 θ = 5–60 °, step width 0.03 °, and scanning speed of 0.0833 °/s.

The diffraction patterns of the neutron-irradiated specimens were collected using a Malvern-PANalytical Empyrean diffractometer equipped with a conventional X-ray tube (Co-Kα, λ = 1.789 Å, 40 kV, 30 mA, line focus) in the transmission mode. An elliptical focusing mirror, a divergence slit of 1/2 °, an anti-scatter slit of 1/2 °, and a Soller slit of 0.02 rad were used in the primary beam. A PIXcel3D detector, attached to a new optical module dCore containing a programmable anti-scatter slit (fixed mode of 1/2 °) and a Soller slit (0.02 rad), was used to measure the diffracted beam. All patterns were collected in the range 2θ = 4–82 ° with a step size of 0.013 ° and a scan speed of 0.0149 °/s. The phases were identified using HighScore Plus software (PANalytical, The Netherlands, version 4.8), including the PDF-4 database (Gates-Rector and Blanton, 2019). For the quantitative analysis of samples, the Profex 4.0.3 software package (Doebelin and Kleeberg, 2015) was used with structural models adopted from the American Mineralogist (Downs and Hall-Wallace, 2003) and COD databases (Gražulis et al., 2009). This program allows for the evaluation of the weight fractions of the crystalline phases using the Rietveld refinement procedure. The specimen was prepared using an oscillating ball mill (MM400, Retsch, Germany) with zirconium oxide balls and stainless-steel milling jars with a zirconium oxide inner coating. An average particle size of 4 μm was achieved. Zinc oxide was used as the internal standard, and 50 % by mass of the specimen was replaced with the target material to quantify the amorphous content.

(6) Water pycnometry

Water pycnometry measurements were conducted using an analytical precision balance (Kern, accuracy 0.1 mg) with a set YDB-03 for density determination. Before the measurements, samples were dried to a constant mass in a drying/heating chamber and removed to cool to room temperature (23–24 °C). Distilled water at room temperature was used as a reference liquid. Three measurements were performed for each sample.

First, the sample was placed carefully on a scale to determine the weight in air; thereafter, the sample was immersed in water at a minimum depth, only to cover the specimen, and the weight was measured. Measures were taken to minimize the bubbles attached to the surface of the samples during water immersion, which may distort the results owing to buoyancy.

The immersion procedure was performed rapidly to avoid the absorption of water by the aggregate, as the surface cracks observed in the specimen, especially after irradiation, can adsorb water. This is further discussed through comparison with other data.

(7) Helium pycnometry

Helium pycnometry measurements were conducted using a Micromeritics AccuPyc II 1340 instrument for the pristine specimens. The same pycnometer model was used in a radiological area located at the Low Activation Materials Development Laboratory (LAMDA) at Oak Ridge National Laboratory (ORNL) for the irradiated specimens. The volume of each sample was measured 15 times and the mean and standard deviation were calculated. To obtain the density of the specimens, the mass was measured using a Metler Toledo balance model ME403E with a precision of 0.0001 g for the pristine specimens, and a Metler Toledo AE100 or a Sartorius ME215P with precisions of 0.0001 g for the irradiated specimens. In the case of measuring

several specimens per irradiation condition, the mean and standard deviations were calculated for the density. Quadratic propagation of errors was considered to estimate the error in the volumetric expansion.

(8) Light optical microscopy

Light optical microscopy of the prepared thin sections of aggregates was used to identify minerals in individual samples and to describe the morphological characteristics of individual minerals, fractures, decomposition, or alteration. The evaluation of textural changes before and after irradiation was of specific interest. For microstructural observation, an optical microscope (Leica DM 2700M), fitted with a 5 Mpix CCD camera, was used.

A slice of thickness 1.5–2 mm (approximate) was cut from the aggregate sample using a low-speed diamond saw (Buehler Isomet Low-speed saw). One side of the sample was affixed to a glass slide using UV cement EpoSpeed S (Struers). After curing, the sample was ground using optically flat 2500 and 5000 grinding wheels and washed carefully. The flat surface was then mounted on a glass slide using the insoluble cement EpoSpeed 20 (Struers), and the fixed upper part was gently released from the soluble UV cement. The Abele system (Struers) was then used for smooth polishing using progressively finer abrasive grit until the sample was approximately 50 μm thick. The final grinding and polishing were performed on a LaboPol 25 machine (Struers) using 2000 grit and a series of diamond suspensions (9, 3, and 1 μm) to finalize the surface to a final thickness of approximately 25–30 μm. The final steps were controlled by observing the prepared thin sections under a polarizing microscope. The method used a Michel–Levy interference color chart. Quartz is typically used as a gauge to determine thickness, as it is one of the most abundant minerals, showing an interference color of first-order gray to white.

(9) Scanning electron microscopy

Scanning electron microscopy (SEM) combined with energy-dispersive X-ray spectroscopy (EDX) was used to characterize the thin sections, dedicatedly prepared for analysis. They were coated with a 25 nm thin layer of carbon (Quorum Technologies Q150T high-vacuum carbon coater) to ensure the conductivity of the surface. SEM imaging, phase identification, and EDX large-area mapping were performed. A scanning electron microscope (SEM, Mira GMU, Tescan) was used to analyze the irradiated samples. The microscope was equipped with the same analytics as the microscope used for non-active aggregate studies: a backscattered electron (BSE) detector for the visualization of the Z-contrast, which enables the differentiation between individual mineral phases present in the sample; an EDX X-MaxN 80 detector (Oxford Instruments) for microanalytical studies; and Aztec 3.3 software (Oxford Instruments) for large-area mapping and data processing. To achieve the maximum BSE contrast and resolution of the mineral phases, an acceleration voltage of 30 kV was used. The working distance was 15 mm during the experiment, and the brightness and contrast of the BSE detector were constant during the imaging. The primary emphasis was on the acquisition of a series of quartz grains and local texture.

Additionally, a large-area map scan was performed. The accelerating voltage was 15 kV, beam current was 3 nA, and the working distance was 15 mm. The individual resolution of the BSE images was 2048 × 2048 pixels, and 36 images were obtained to cover an area of 200 × 200 μm^2. EDX mapping was performed for this process. To analyze the crack development

characteristics, an image analysis using Python code was performed. The processes are as follows: 1) contrast correction (thresholding), 2) classification of each pixel into four different types (dark, dark gray, light gray, and whitish areas), 3) segmentation, 4) skeletonization, and 5) statistical evaluation. In this process, a crack is defined as a continuous area containing crack pixels. Crack size is defined as the number of pixels included in the crack. The crack length counts all pixels of the crack skeleton, that is, the longest path in the skeleton, as well as all pixels in the skeleton branches. The medial axis (skeleton) is the set of all points with more than one closest point on the object boundary, and for each point, we considered the closest point distance as the width, as shown in Fig. 3.

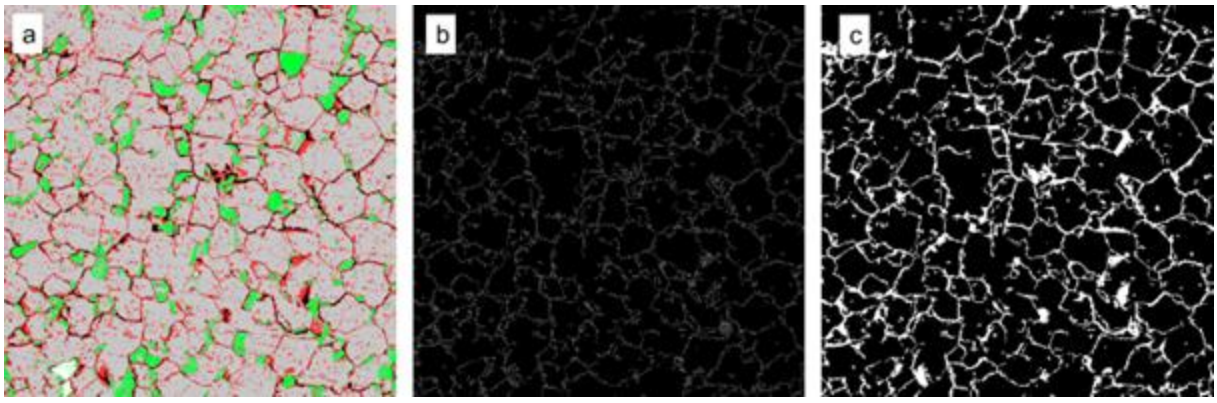

Fig. 2 Image analysis steps shown for selected BSE image of sample PPT-E. Thresholding (a), skeletonization (b), and the resulting mask of the detected cracks (c).

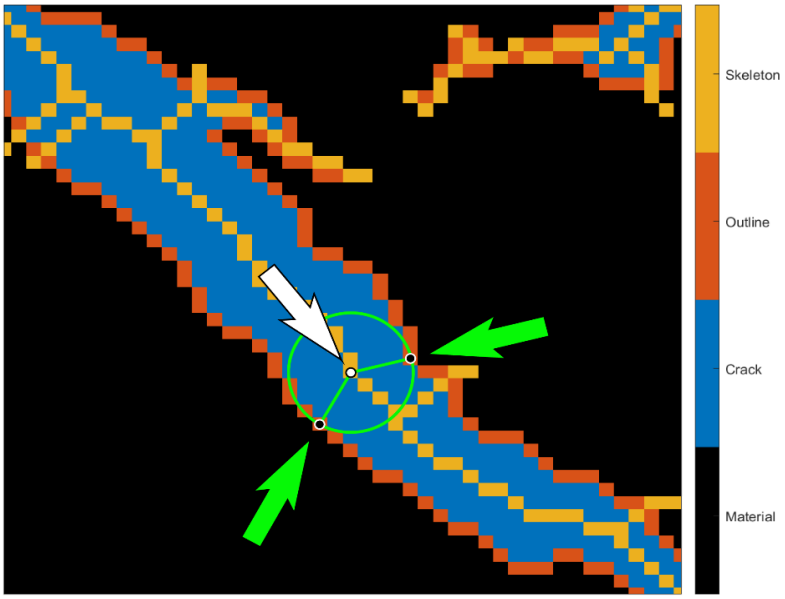

Fig. 3 Graphical representation of the determination process of crack width and crack (blue). The boundary pixels are colored in red and skeleton in amber. One of the skeleton points is shown with the closest points and the circle emphasizing the distance.

3. Experimental results

3.1 Gamma-ray irradiation

(1) Temperature

The temperature measurement results are shown in Fig. 1. The temperature varied from 10 to 50 °C. As the room temperature was not controlled, seasonal variation was clearly confirmed. Based on this data, the temperature history of the companion heating experiment was determined. The temperature histories of the heating experiment for the 27 MGy, 55 MGy, and 108 MGy equivalents are summarized in Fig. 5. The specimens for the companion heating experiment were placed in a heating chamber with these temperature histories.

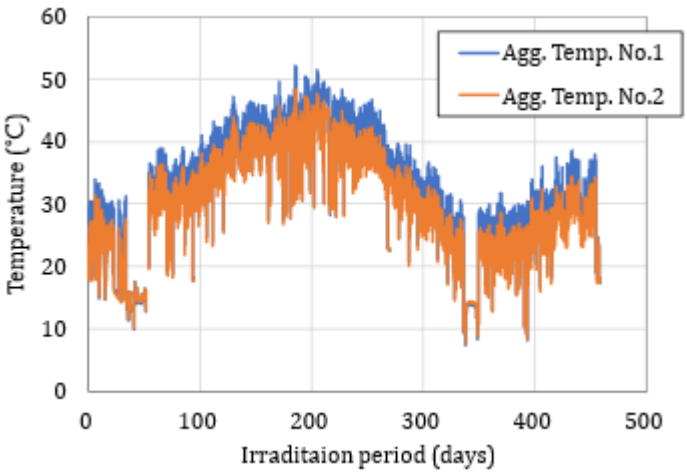

Fig. 4 Temperature of aggregate specimen during gamma-ray irradiation. Location of specimen No. 1 is the surface nearest to the gamma-ray source, and that of No. 2 is opposite the surface of the specimen.

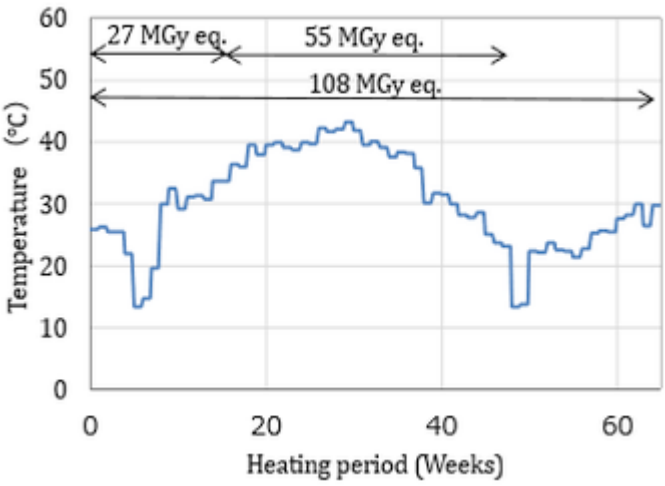

Fig. 5 Temperature history data for companion heating experiment.

(2) Physical property changes

Figure 4 shows the physical property changes of the aggregate specimens. Fig. 6 (a) shows the dimensional changes. In this case, a slight increase in the specimen size was confirmed in both heating and gamma-ray irradiation cases. However, the size change was at most 0.18% in length, and would not be detrimental in irradiated concrete in which the thermal expansion coefficient

of mortar is larger than that of coarse aggregate, resulting in no volume mismatch in the concrete. Fig. 6 (b) shows the mass changes of the specimens. As the irradiation period or heating period progressed, the decrease in mass was more pronounced. The irradiation specimens showed larger mass loss than when heating the specimens for the same experimental period. The mechanism of the slight expansion was not clear; however, the possible explanation include: 1) the expansion of rock-forming minerals owing to gamma-ray irradiation and 2) the loss of water-induced cohesion between rock-forming mineral grains owing to drying. Based on the expansion in either case, the latter mechanism may be dominant, however, further investigation is necessary for clarification.

The compressive strength results are shown in Fig. 6 (c). The longer the experimental period, the larger the increase in compressive strength, except for the data anomaly for the 55 MGy equivalent heating. The mass loss shown in Fig. 6 (b) can be explained by the increase in the surface energy because of drying (Martin, 1966; Ojo and Brook, 1990; Wong et al., 2016). In contrast, the Young's modulus of the rock was not significantly changed by gamma-ray irradiation and equivalent heating, except for the data anomaly for 108 MGy gamma-ray irradiation. In addition, a sudden temperature increase to 65 °C, which may cause cracks on the surface because of a temperature gradient inside the specimen, did not affect the compressive strength and Young's modulus.

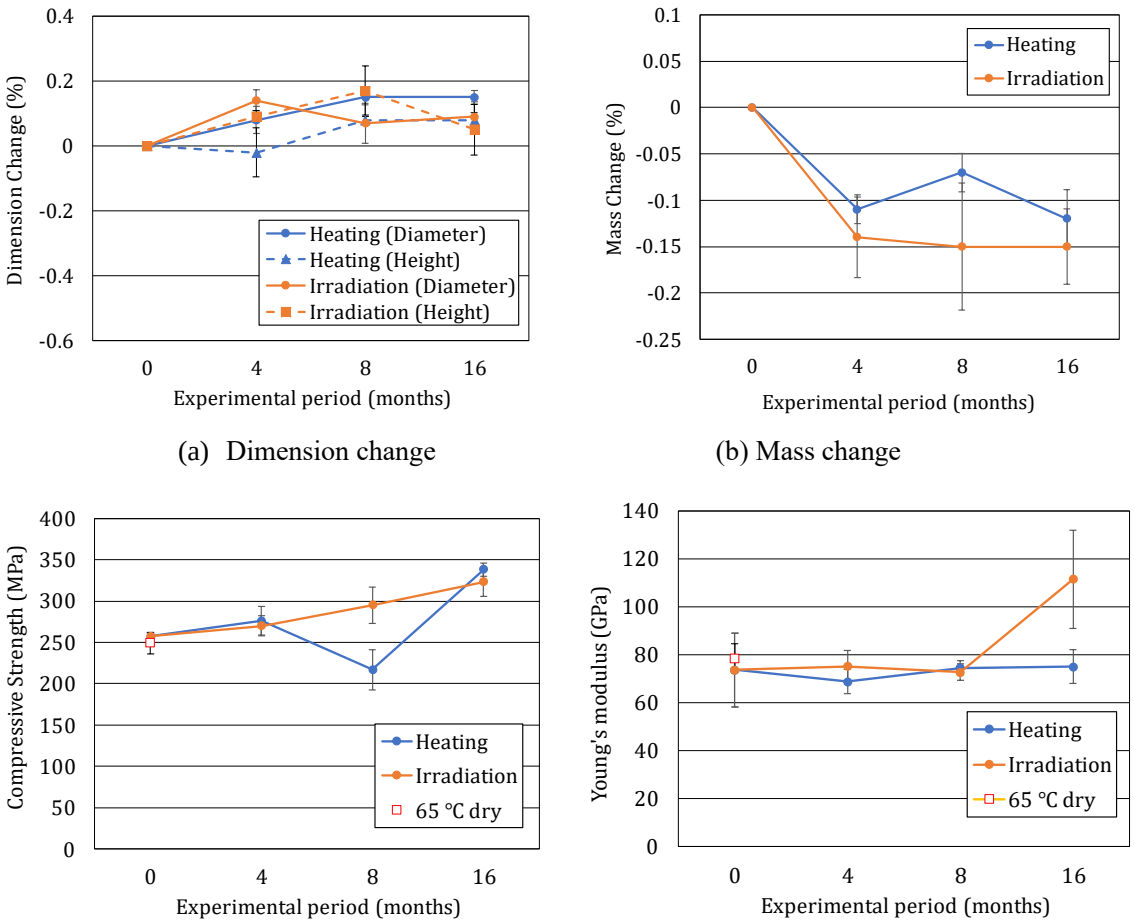

(a) Dimension change (b) Mass change

(c) Compressive strength (d) Young's modulus

Fig. 6 Physical property changes of the meta-chert aggregate specimens: (a) dimension change, (b)

compressive strength, and (c) Young's modulus. The data at experimental period = 0 months corresponds to the non-irradiated specimen. 4, 8, and 16 months of experimental period correspond to the gamma-ray doses of 27, 55, and 108 MGy, respectively. The data was partially adopted from Maruyama et al. (2017).

(3) XRD

By performing Rietveld refinement of the obtained XRD patterns, the lattice parameters of α-quartz were identified. The lattice parameters were confirmed to increase, as the gamma-ray dose and heating period increased. The results are summarized in Fig. 7. By comparing the data of gamma-ray irradiation and heating, it can be concluded that heating-related relaxation of α-quartz may introduce the expansion of the α-quartz. It is possible that ionization influences the change in the lattice parameters, as suggested by Lue et al. (2020), however, this mechanism cannot be dominant, because the secondary impact of neutrons is not efficient.

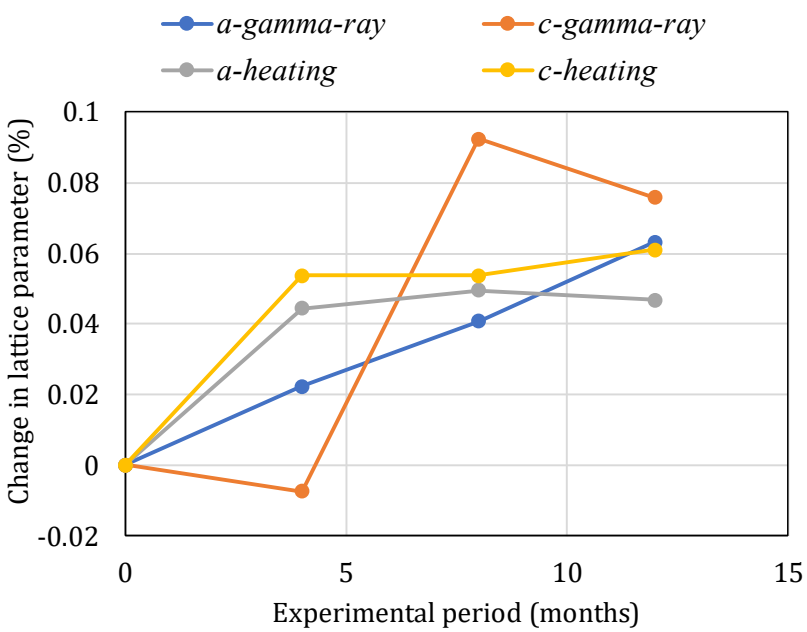

Fig. 7 Change in Lattice parameters of α-quartz because of gamma-ray irradiation.

3.2 Neutron irradiation

(1) LOM analysis

The LOM results are listed in Table 4. Two images with different magnifications are shown for each neutron fluence. The meta-chert specimen was typically highly fine-grained with alternating parts of a coarser-grained texture. Fractions of the aggregate exhibited trace alterations, such as the presence of veins filled with secondary micas and clinochlore. Some specimens exhibited laminar textures. Quartz veinlets are generally abundant. In the lower magnification images, cracks were observed in the high neutron fluences, particularly for PPT-E.

For the larger-magnification images, we focused on regions where fine quartz grains

were observed. In the images with larger magnification, pores with the size of 0.1−30 μm were confirmed. For PPT-D and PPT-E, cracks were visible at the grain boundaries. These cracks are discussed in detail using the SEM images in section 3.2 (4).

There were no clear changes in the optical properties, such as amorphization and undulous extinction, of quartz. Large amounts of pyrite (bright spots in the reflected light) were observed in some aggregates.

Table 4 Results of plane polarized light optical microscope images (left), fine-grained areas in reflected light are shown on the right.

Non Irradiated	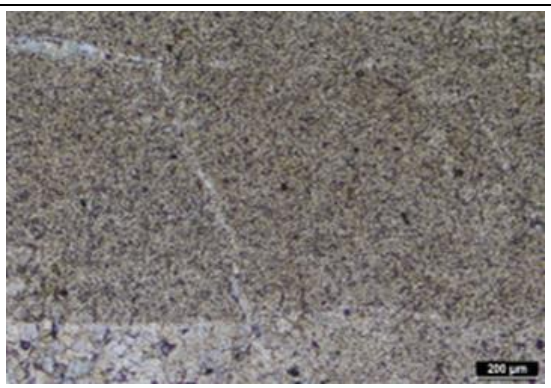	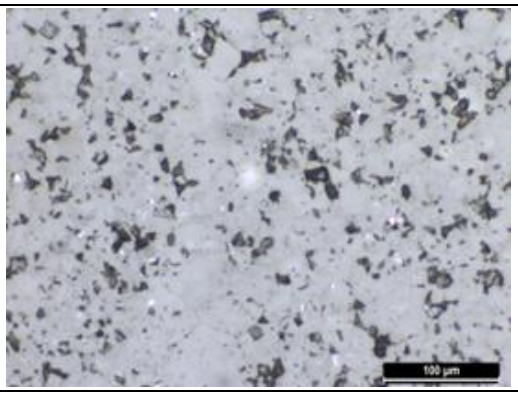
PPT-B	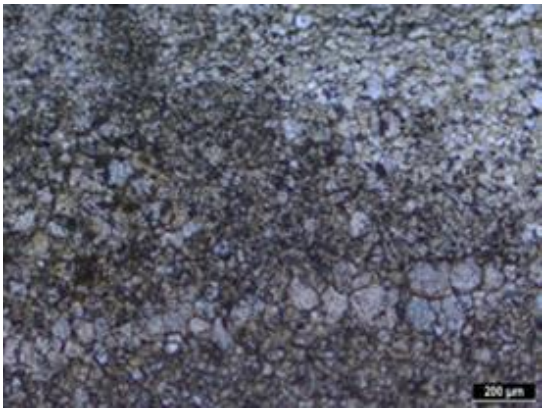	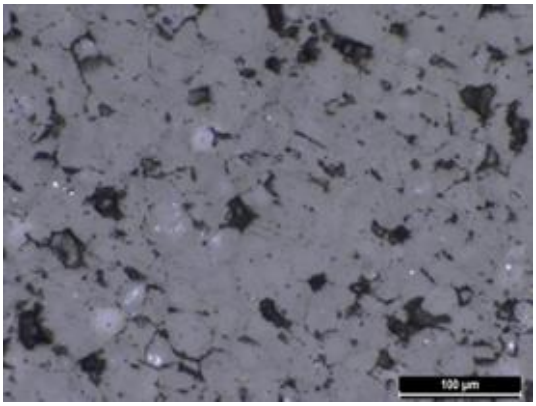
PPT-C	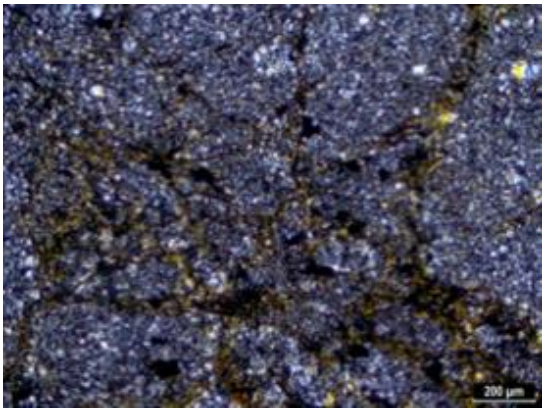	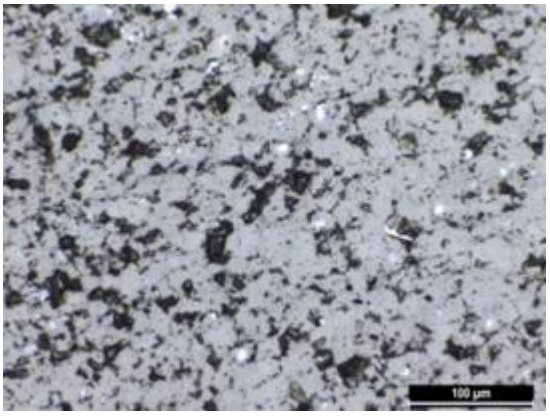

PPT-D	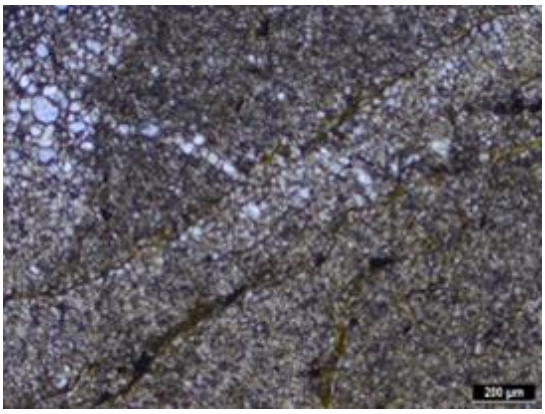	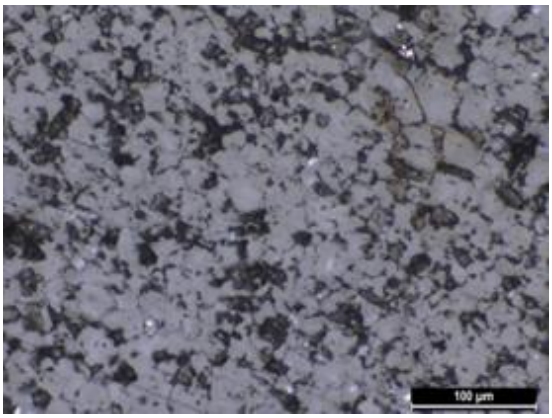
PPT-E	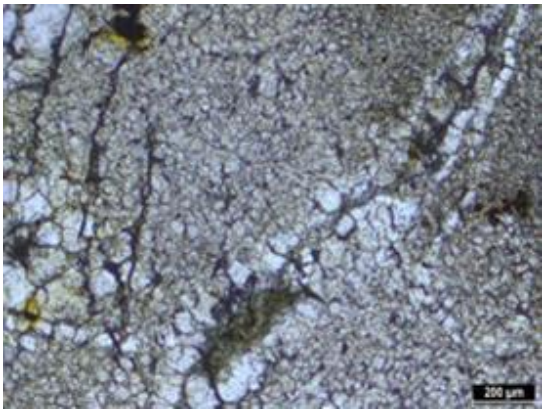	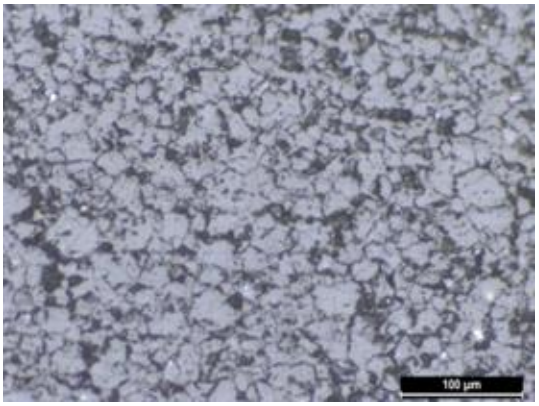

(2) Dimension change

The dimensional changes in the specimens were obtained, based on which the volume expansion ratio was calculated. The volume expansion ratio was plotted as a function of neutron fluence, with the data for α-quartz compiled by Bykov et al. (1981) in Fig. 8. Based on the original figure presented by Bykov et al., the threshold value of 0.01 MeV was used. As shown in Fig. 8, the obtained data were consistent with previous αquartz data. Even though the mass content of α-quartz was approximately 90%, the data still agreed significantly.

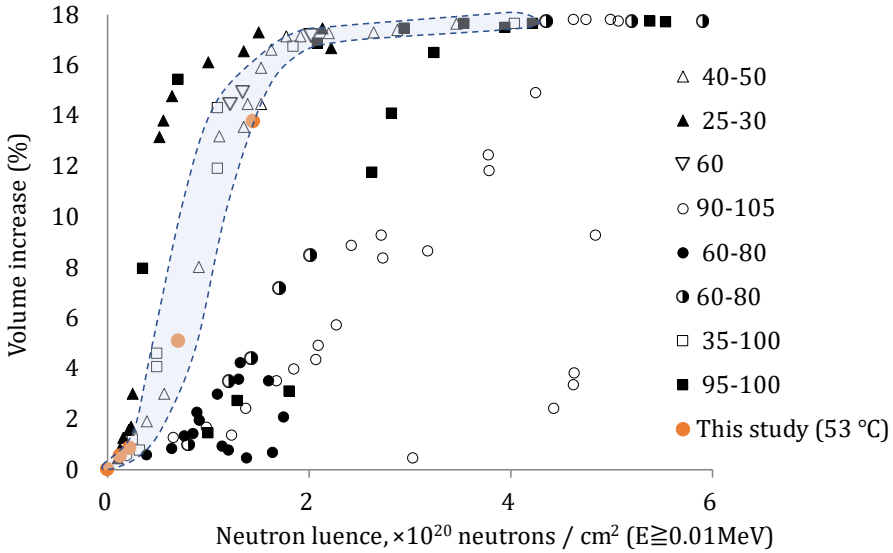

Fig. 8 Relationship between the volume expansion ratio of meta-chert and neutron fluence (E ≧ 0.01 MeV). The legend shows the average or range of temperature during neutron irradiation in °C. The dotted lines were plotted manually through visual judgement.

Water pycnometry data were also obtained in this study. It was observed that water permeated into the specimens through connecting pores and cracks, especially in cases where the specimen possessed fine cracks because of neutron irradiation. To confirm this, the volume expansion ratio calculated by the density change of the specimens measured by the water pycnometry was compared using the dimensional change data in Fig. 9. For this calculation, first, the density obtained by mass and dimensional measurement were calibrated according to the density measured by the water pycnometry for the unirradiated specimens. The density of the pristine specimens obtained by water pycnometry was calculated using the calibration. Finally, the volume expansion was determined by using the density of the water pycnometry of irradiated specimens and the density from the water pycnometry of the pristine specimens were calculated. The helium pycnometry data were treated similarly.

Not all the pores and cracks were filled with water in the case of water pycnometry; however, they were completely filled with helium in the case of He-pycnometry. The impact of cracks can be visualized by comparing the volumetric expansions calculated from water and He-pycnometry, with the dimensional volume expansion. A comparison is shown in Fig. 9. In

general, the volume expansion ratios of the dimensional change measurements were always larger than those of the water pycnometry measurements. The He-pycnometry results were the smallest. This suggests that the cracks caused by neutron irradiation may influence the volume change from a considerably low neutron fluence range. In addition, the discrepancy increased from PPT-C (2.19E+19 n/cm^2, (E≧0.01 MeV)) to PPT-D (6.99E+19 n/cm^2, (E≧0.01 MeV)), and became the largest for PPT-D. Thereafter, the discrepancy decreased for PPT-E (1.43E+20 n/cm^2, (E≧0.01 MeV)).

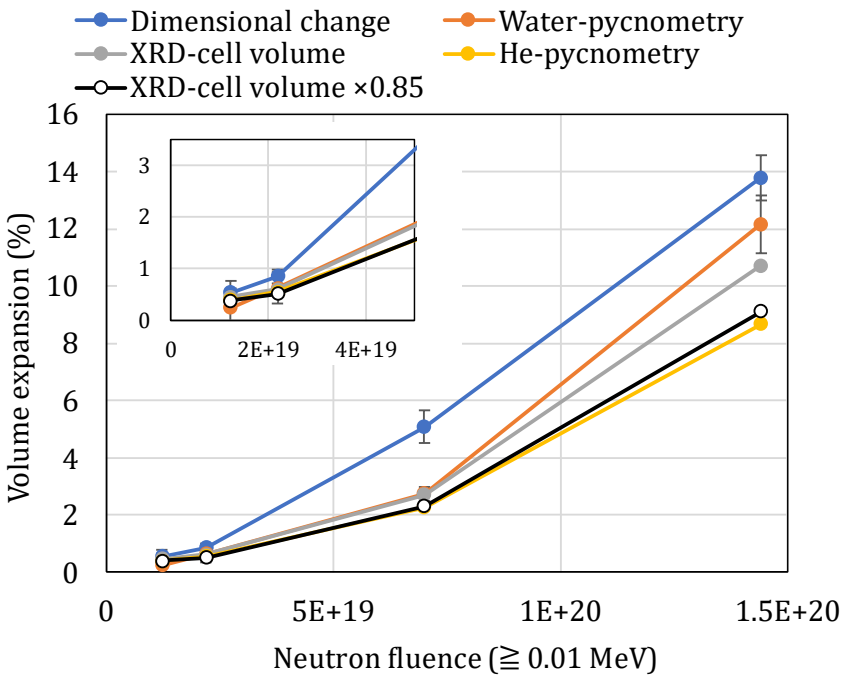

Fig. 9 Volume expansion ratio of meta-chert obtained by dimension change measurement, water pycnometry measurement, and He-pycnometry measurement, as a function of neutron fluence. Quartz cell volume expansion obtained by X-ray powder diffraction (XRD) measurements are also plotted.

(3) XRD analysis

To understand the impact of neutron irradiation on the crystal structure, XRD was performed. The XRD charts are summarized in Fig. 10. The pristine αquartz showed lattice parameters, a = 4.914(1) and c = 5.405(1), which are quite similar to other reported values for α-quartz (Wittels, 1957; Silva et al., 2018). As confirmed by Fig. 10, the α-quartz peaks became smaller and shifted to larger d spaces as the neutron fluence increased.

Lattice parameters and cell volumes were calculated using the Rietveld refinement method. The results are presented in Table 5. The lattice parameters, a and c, increased as the neutron fluence increased, as shown in Fig. 10. These behaviors are illustrated in Fig. 11. The order of the changes was consistent with previous studies (Wittels, 1957; Silva et al., 2018). As indicated by Silva et al. (2018), flux appeared to influence the rate of increase in the lattice parameters. To obtain a deeper understanding, Rietveld phase quantification was performed. The results are summarized in Table 6. It was confirmed that the α-quartz became partially X-ray amorphous, and the quantified crystallinity decreased as the neutron fluence increased, whereas the amorphous content increased.

The cell volume increase ratio was calculated and compared to the expansion of the aggregate, as shown in Fig. 9. Interestingly, the expansion of the cell volume was consistent with the volume expansion measured by He-pycnometry. This was observed in a previous work by Wittels (1957). In the lower neutron fluence range (approximately 3×10^{19} n/cm^2, E ≥ 0.05 MeV), the volume expansion of the cell was elastic and consistent with the nominal volume expansion of the specimen. In the current study, the volume expansion of the α-quartz cell and the nominal volume expansion of the specimen at neutron fluences ≤ 6.99×10^{19} n/cm^2, at E ≧ 0.01 MeV were similar for He-pycnometry data and 0.85 × XRD-cell volume, considering the α-quartz content in the aggregate). At the largest neutron fluence, a marginal difference between the He-pycnometry data and the 0.85 × XRD-cell volume was confirmed. This trend was consistent with the observations of Wittels (1957).

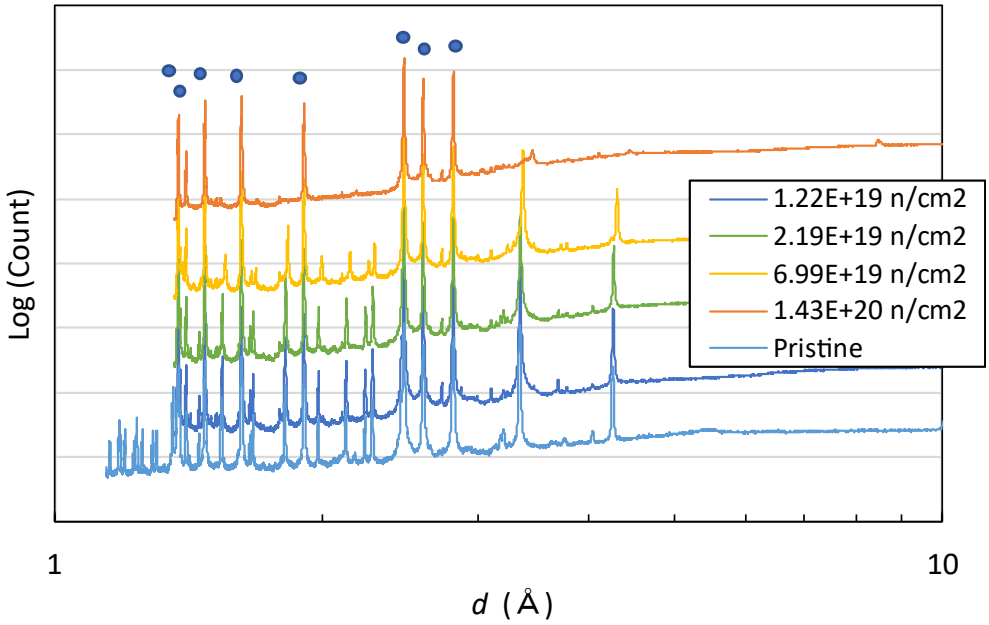

Fig. 10 XRD results for irradiated and non-irradiated specimens. Blue marks indicate the peaks of internal standard.

Table 5 Irradiation condition and lattice parameters of irradiated and non-irradiated specimens.

	Irradiation condition		Lattice parameter		Cell volume	Volume increase
	≧0.1 MeV	≧0.01 MeV	*a* (Å)	*c* (Å)	(Å^3)	(%)
Pristine	0	0	4.914(0)	5.406(0)	113.11	0
PPT-B	7.63E+18	1.22E+19	4.925(0)	5.410(0)	113.63	0.455
PPT-C	1.39E+19	2.19E+19	4.928(0)	5.411(0)	113.80	0.606
PPT-D	4.45E+19	6.99E+19	4.974(0)	5.423(0)	116.17	2.705
PPT-E	9.04E+19	1.43E+20	5.135(0)	5.486(0)	125.23	10.715

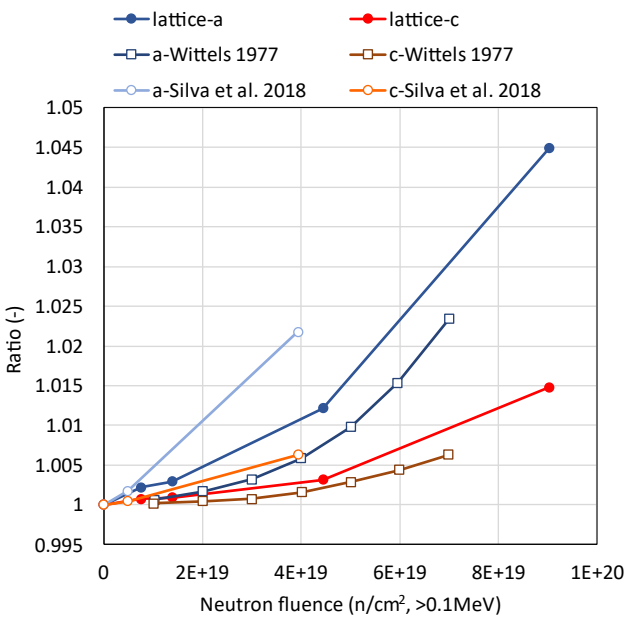

Fig. 11 Change in Lattice parameters, ***a*** and ***c***, caused by neutron irradiation.

Table 6 Quantification of phases in pristine and irradiated specimens through Rietveld analysis.

	Pristine		PPT-B		PPT-C		PPT-D		PPT-E	
	Value (%)	1σ (%)	Value (%)	1σ (%)	Value (%)	1σ (%)	Value (%)	1σ (%)	Value (%)	1σ (%)
Quartz	86.69	2.61	84.63	1.79	73.23	0.57	44.40	1.03	5.83	0.76
Amorph.	5.36	1.85	8.87	2.01	15.27	0.83	44.90	1.08	79.27	2.83
Chlorite	0.90	0.34	0.62	0.40	0.77	0.40	1.02	0.37	0.87	0.21
Microcline	1.42	0.35	3.68	0.56	3.40	0.30	6.08	0.34	3.40	0.51
Anorthite	3.13	1.71	1.07	0.41	4.70	0.20	1.78	0.38	2.53	0.24
Biotite	1.32	0.84	1.10	0.31	1.83	0.20	1.48	0.51	5.08	1.42
Other	1.18	0.22	-	-	0.83	-	0.3	-	0.06	-
Rwp	6.39-14.76		6.42-8.56		5.90-6.64		6.55-7.56		4.22-5.23	
Rexp	3.93-8.35		2.92-3.09		2.67-2.71		2.61-2.68		1.84-1.88	
GOF	1.64-1.80		2.16-2.83		2.19-2.37		2.50-2.82		2.28-2.80	

Assuming that only the volumes of α-quartz and the amorphous phase were affected by neutron irradiation, the following equation was used to estimate the volume change of the amorphous phase:

$$M_q \cdot \Delta V_q + M_A \cdot \Delta V_A = \Delta V \quad (1)$$

where M_q, and M_A are the normalized mass of α-quartz and amorphous aggregate, respectively (g/g—agg); and ΔV_q, and ΔV_A are the volume expansions of α-quartz and

amorphous aggregate, respectively (m^3/m^3); ΔV is the volume expansion of the aggregate specimen determined by He-pycnometry measurements. The density of the original amorphous content found in the pristine aggregate was assumed to be the same as that of αquartz.

Fig. 12 shows the calculated results. As expected from a previous study (Nakano et al., 2005), the X-ray amorphous phase did not possess a constant density. The calculated density of the X-ray amorphous phase of α-quartz in the current study was approximately equal to that of the irradiated αquartz. In the current irradiation experiment, two different processes of volume expansion of neutron-irradiated αquartz,: first stage, where the volume increase determined by X-ray and hydrostatic methods are equal; and a second stage, where the volume change indicated by X-ray measurements is larger than the bulk volume change determined hydrostatically; do not apply. This is significant from the perspective of aging management. If a core specimen can be sampled from locations that are exposed to neutrons, it is possible to evaluate the volume expansion of quartz grains using XRD/Rietveld analysis.

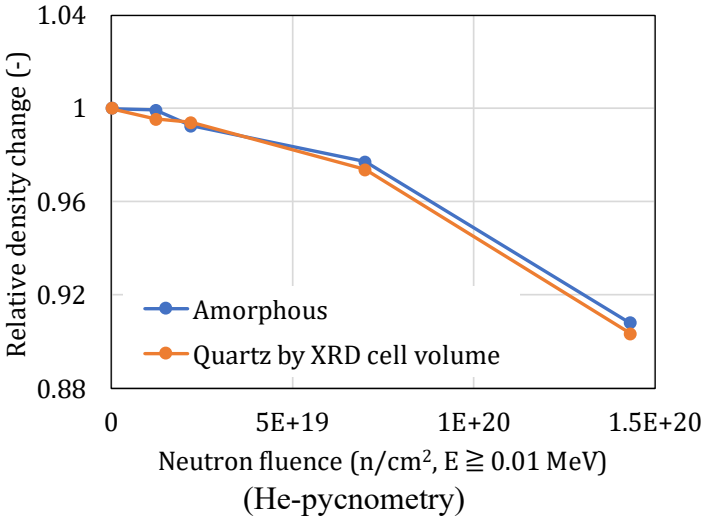

Fig. 12 Relative density change of α-quartz and amorphous phase calculated by assuming that other phases do not contribute to the volume change of aggregate.

Finally, the crystallinity index of the α-quartz was determined. It is well established that quartz crystallinity can be evaluated from the peak at $d(212)$ (d = 1.3820 Å), the ratio of the peak height (observed at approximately 2θ = 67.74 ° Cu Kα) to the peak height from the adjacent value (observed at approximately 2θ = 67.8 ° Cu Kα) in the quintuplet (Murata and Norman, 1976). This index was applied in this study, and it was found that the impact of irradiation can be evaluated using this method. As shown in Fig. 13(a), the peaks became unclear as the neutron fluence increased and the crystallinity weakened. The crystallinity index as a function of neutron fluence is shown in Fig. 13(b). A monotonic decrease was confirmed as a function of neutron fluence. This method can be applied to real structures as well. If two core specimens are sampled from two locations of the target reinforced concrete member affected by neutron irradiation, one in the irradiated region and the other in the non-irradiated region, it is possible to evaluate whether the alpha-quartz in the neutron-irradiated region is affected by neutrons.

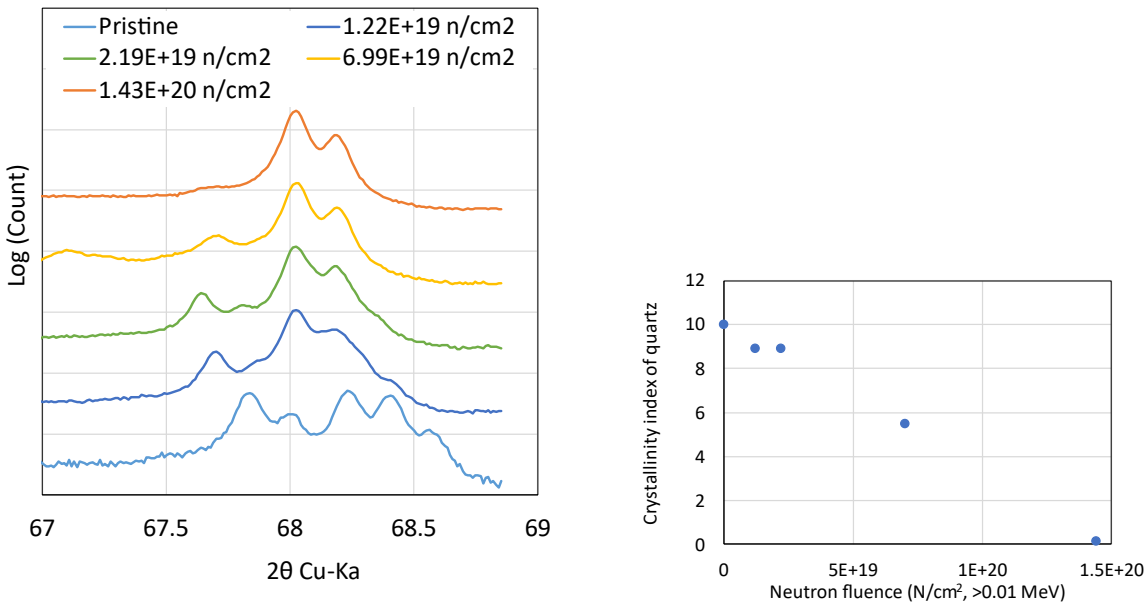

(a) XRD chart around 68 °. (b) Crystallinity index.

Fig. 13 (a) Quintuplet of irradiated specimens observed from $2\theta = 67.5–68.5$ ° Cu Kα (Converted from Co- Kα) and (b) the calculated results of the crystallinity index of α-quartz.

(4) SEM analysis

The SEM-BSE images are shown in Fig. 14. As the neutron fluence increased, the boundary of the α-quartz grains became apparent, and the observed crack area increased. The gray darkness of the α-quartz became brighter, which was unexpected, given the decrease in the density of the alpha-quartz. This occurred because of the neutron-induced activation of the materials. Crack development was qualitatively analyzed using image analysis within a large mapped area, and the results are summarized in Fig. 15–Fig. 17.

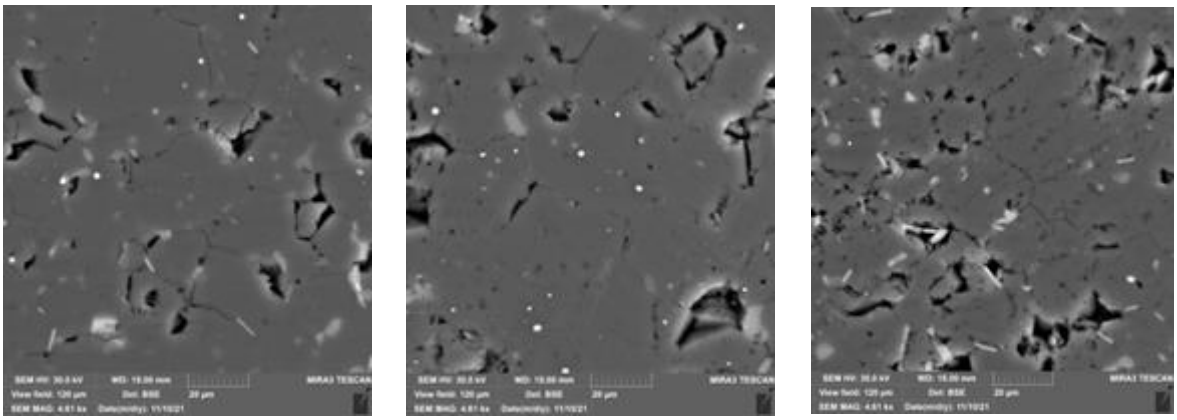

(a) Pristine (b) PPT-B (c) PPT-C

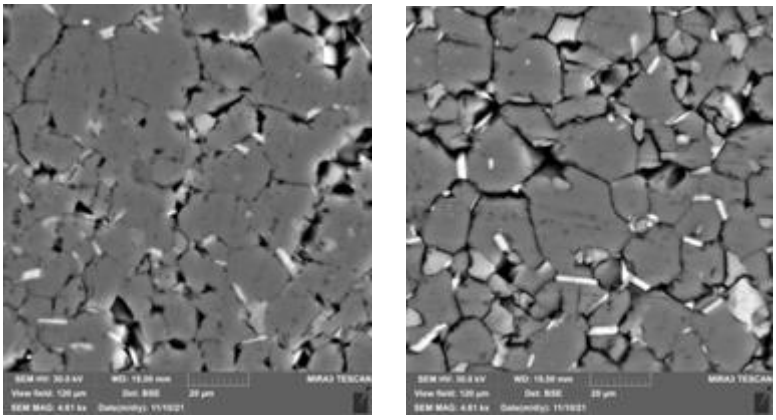

(d) PPT-D (e) PPT-E

Fig. 14 Scanning electron microscopy–backscattered electron (SEM–BSE) images of non-irradiated and irradiated samples.

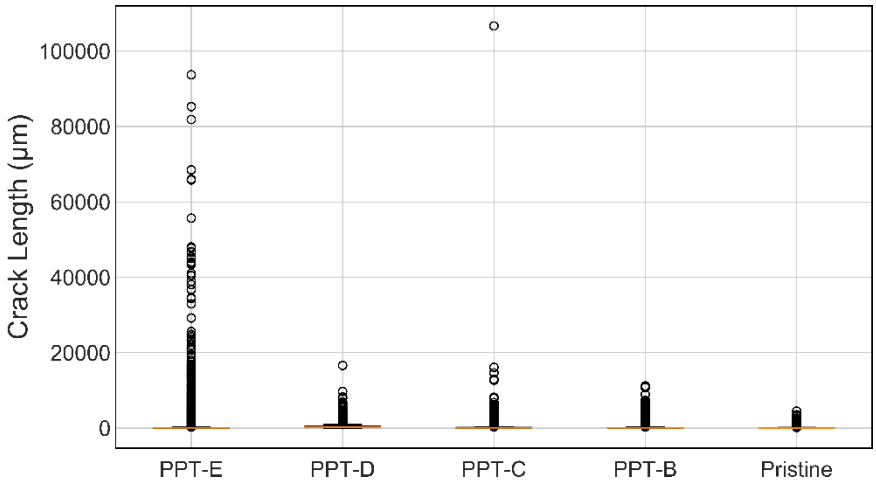

Fig. 15 Length of cracks in 200 × 200 μm^2 area of the irradiated and non-irradiated specimens.

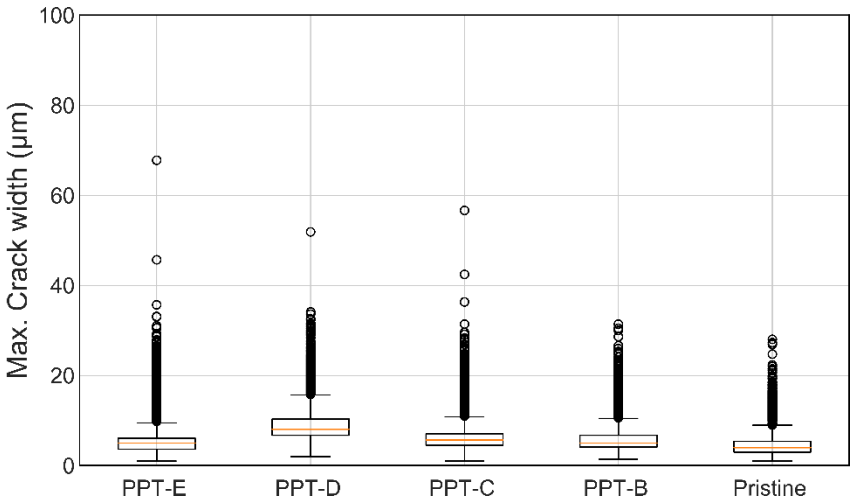

Fig. 16 Maximum crack width of cracks in 200 × 200 μm^2 area of the irradiated and non-irradiated

specimens.

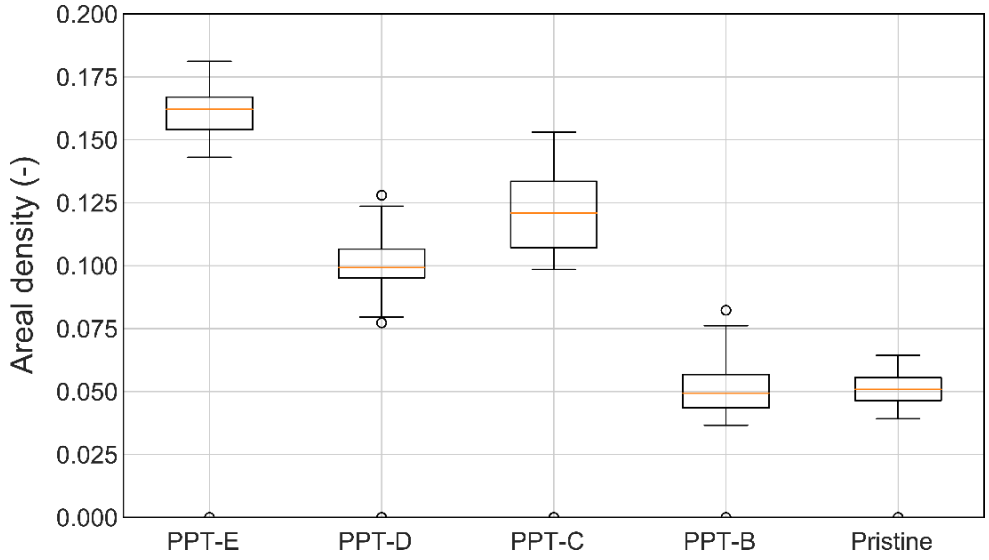

Fig. 17 Crack area density in a surface area of 200 × 200 μm^2 in the irradiated and non-irradiated specimens.

Fig. 15 shows the lengths of the cracks in the specimen. Some initial cracks existed in the pristine specimen; however, the impact was minor. As the fluence increased, the maximum crack length significantly increased. This indicates that the cracks became interconnected as the quartz expanded. The expansion ratio depends on the orientation of the crystal structure, as confirmed by Fig. 11, and the direction of the lattice parameter, *a*, was observed to be more sensitive than that of the lattice parameter, *c*. As the crystal direction was almost randomly distributed, as confirmed by cross-polarized microscopy observations, cracks could start from the grain boundaries, where the orientation of neighboring grains is different. For low doses (Fig. 14(a) and (b)), cracks were localized between neighboring grains of different orientations, and their lengths were not significant; the crack length was approximately equal to the grain edge length. After the continuous expansion of the grains, the cracks widened, and the length increased because of interconnection. As confirmed by Fig. 16, the crack width gradually increased with neutron fluence. An exception was observed for PPT-E. In this case, as shown in Fig. 14, approximately all the grain boundaries were detached and the length of the cracks increased significantly. Owing to this length change, the crack width decreased according to the calculation. The total crack area shown in Fig. 17 provides a more appropriate insight. The pristine and PPT-B samples showed similar crack area densities, although, for PPT-B, the distribution was marginally shifted toward a larger area density. The original natural porosity was included in this value. The PPT-C and PPT-D samples showed approximately 7.4 % and 5.0 % crack area increases, respectively. This PPT-C value is difficult to explain. In Fig. 9, PPT-C showed a similar expansion of cell volume, dimensional aggregate expansion, and expansion

measured by water pycnometry, and there was no indication that cracks exerted any influence on the aggregate expansion. PPT-D showed a 2.8 % larger dimensional aggregate expansion than that measured using He-pycnometry. However, this difference was lower than the 5.0 % increase in the crack area. This can be explained through several factors. The most plausible explanation is that the SEM images were captured in a region where fine-grained α-quartz was observed, and there was another region, that is, vain and deposited α-quartz, where a different crack pattern might have occurred. Therefore, the overall trend may not be consistent with the local observational results. In addition, the two-dimensional evaluation effects and stress release impact, resulting from sample cutting and polishing cannot be excluded.

The PPT-E sample showed a 5.1 % difference between the dimensional expansion and the expansion evaluated by He-pycnometry. Based on these data, it appears that the crack impact increased, and this trend was reproduced with an SEM crack area density increase of 11 %. This value was marginally lower than the total volume dimensional expansion of 13.8 %. As the density change of α-quartz was more than 10%, the crack impact of the PPT-E sample was also overestimated.

This discussion indicates that this SEM image analysis cannot be used for the quantitative evaluation of the crack development in the aggregate, because of neutron irradiation. However, this method can yield qualitative information. Thus, cracks can be concluded to be formed because of neutron irradiation, deteriorating the aggregate integrity.

4. Discussion

A multi-scale study was conducted to understand aggregate behavior based on the behavior of mineral grains. With respect to the grain size, the orientation of the crystal structure exerted a large influence on the volume expansion, and the lattice parameter, a, was more sensitive than c, which has been confirmed in previous studies (Johnson and Pease, 1954; Wittels, 1957; Primak, 1958; Denisov et al., 2012; Silva et al., 2018). The ratio of the expansions along the a and c axes are given by $\Delta a/a_0/\Delta c/c_0$, respectively, where a_0 and c_0 are the original crystal sizes of α-quartz in the directions of the a and c axes, respectively, and Δa and Δc are the expansion of the crystal structure in the directions of the a and c axes, respectively. The ratios were calculated to be approximately 3.0. This value was similar to that reported by Wittels (1957). As the final amorphized material exhibits an isotropic property (Primak, 1958; Douillard and Duraud, 1996). the calculation result should be $1+(\Delta a/a_0)=1.088$ and $1+(\Delta c/c_0)=0.990$, assuming that total volume expansion was 17.4 %, as discussed by Primak et al. (Primak et al., 1955; Primak, 1958). If there was no contraction in the c-direction, a 21 % volume increase was required to satisfy the isotropic condition. As the XRD chart shows a continuous expansion in the a- and c-directions, a different behavior should occur in the amorphous phase. To visualize this trend, the cell volume expansion and $(\Delta a/a_0)/(\Delta c/c_0)$ were compared with those of $1+(\Delta c/c_0)$ and $1+(\Delta a/a_0)$, as shown in Fig. 18. It was confirmed that $(\Delta a/a_0)/(\Delta c/c_0)$ shows a peak

at 6.99 × 10^{19} n/cm^2, E ≧ 0.01. Following the discussion by Wittels (1957), in our measurement, the structure detected by XRD in the neutron fluence range ≤ 6.99×10^{19} n/cm^2, E ≧ 0.01 MeV, showed elastic deformation caused by the dislocation of atoms because of neutron irradiation. In this range, the amorphous X-ray structure also shows a similar density change, as shown in Fig. 12. We inferred that probably, the structural difference is less significant from the perspective of density. Moreover, the behavior changes and the structure shifted to an isotropic condition.

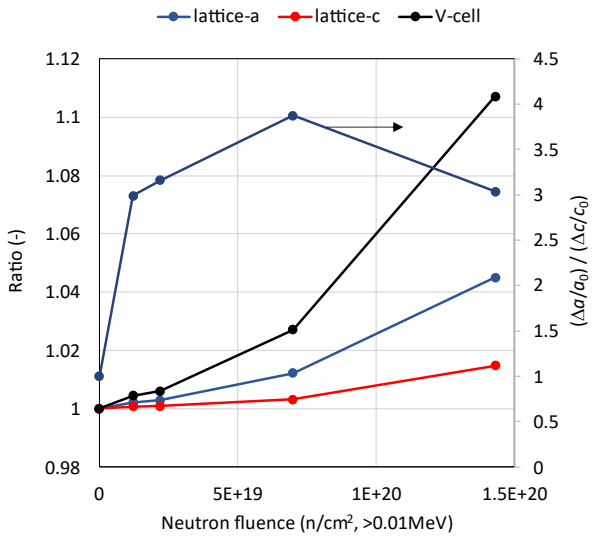

Fig. 18 Comparison of 1+ ($\Delta c/c_0$), 1+ ($\Delta a/a_0$), cell volume expansion ratio, and ($\Delta a/a_0$)/($\Delta c/c_0$).

In previous studies, the amorphization process (the relationship between maximum normalized damage (amorphized) and neutron fluence, and damage degree was generally detected using the Rutherford backscattering technique) under ion irradiation was best fitted by the nucleation and growth model (Bolse, 1999). This suggests that amorphization developed surrounding the nucleation of amorphization in the crystalline regions. In the crystalline region of zircon, which was amorphized by collision cascades or the overlapping of collision cascades, crystalline islands were found to be slightly rotated with respect to each other (Weber et al., 1994). These experimental data support the concept of the nucleation and growth model; however, in this model, there was no detailed discussion on the properties of the amorphized region, such as density. Similarly, by using indentation hardness data, ion-irradiated sample alteration was modeled with a three-phase model (Nakano et al., 2005), assuming a crystalline region, an intermediate transition phase, and a final amorphized phase. This model can predict the volume expansion of neutron-irradiated αquartz (Maruyama et al., 2017a) by assigning intrinsic densities to the three phases. Additionally, the definition of the amorphized region by the models and experimental techniques was not consistent. In this study, powder X-ray diffraction measurement detected the loss of long-range correlation, considering that the

densities of the crystalline region and the amorphized region were approximately identical, which does not correspond to the assumptions of the three-phase model. In the amorphization process, the crystalline region and amorphized region were gradually and similarly expanded, probably showing similar local structures and loss of long-range correlation (which is referred to as topological disordering (Gupta, 1993; Hobbs, 1995)), by the rotation of Si-O-Si bonds.

Defects or small cracks in the α-quartz grains can be observed in Fig. 14(d) and (e). The magnified image is shown in Fig. 19. This further indicates the structural symptoms of the system shifting toward isotropic conditions.

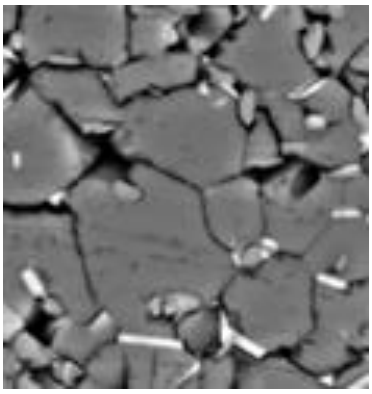

Fig. 19 Close-up of the Fig. 14(d). The cracks, voids, and defects were confirmed in the α-quartz grains. The image size is approximately 40 × 40 μm^2.

This local crystal-scale behavior influences the aggregate expansion. The crystal structure orientation of the grains was different; the stress was accumulated at the grain boundaries. This stress should be > 100 MPa, considering the strain of percent order and Young's modulus of αquartz; therefore, detaching or cracking at the grain boundary was easily formed. This was confirmed by both the LOM and SEM results. However, as discussed earlier, the observed crack width could be overestimated with respect to the actual condition. Qualitative consistency was confirmed based on volume expansion data and microscope observations. The volume change mismatch between the data obtained by dimensional change measurements and He-pycnometry measurements suggested that the crack opening contributed toward volume expansion for doses ≥ the neutron fluence of 2.19E+19 n/cm^2 (E ≧ 0.01 MeV). It was assumed that the discrepancy in PPT-B between the He-pycnometry data and dimensional change was associated with the intrinsic aggregate pores. The ratio of contribution of solids and cracks to the volume expansion by solids and cracks are summarized in Fig. 20. The crack contribution was observed to increase with neutron fluence up to 6.99E+19 n/cm^2 (E ≥ 0.01 MeV). At the maximum neutron fluence, the contribution of cracks was lower than that for 6.99E+19 n/cm^2 (E ≥ 0.01 MeV). This trend can be explained by the change of irradiated αquartz into isotropic amorphous quartz and a homogenous volume expansion that might mitigate the crack opening. This could be substantial

from the perspective of the aging management of concrete structures, specifically, its contribution to the volume expansion of the aggregate.

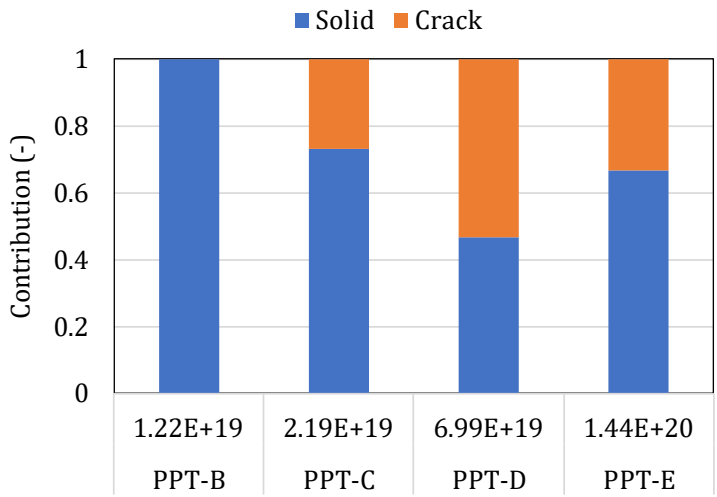

Fig. 20 Contributions of solids and cracks to volume expansion of aggregate.

5. Conclusion

Concrete aggregate cored from meta-cherts were irradiated with neutrons and gamma-rays. The results are as follows.

1) Gamma-ray doses of up to 108 MGy did not significantly influence the physical properties of the aggregate.
2) The volume expansion caused by neutron irradiation, observed through dimensional measurement, water pycnometry, and He-pycnometry were 13.8 %, 12.2%, and 8.67%, respectively. The crack opening inside the aggregate explained the difference between the dimensional measurement data and pycnometry data.
3) The density change obtained by He-pycnometry was consistent with the cell volume expansion measured by XRD/Rietveld analysis.
4) The cracks between quartz grains were confirmed by both LOM and BSE microscopy observations. However, the crack opening area analyzed by image processing was overestimated when compared to the volume increase data.
5) The XRD data of the irradiated specimens suggested that the X-ray amorphous phase exhibited a density similar to that of the irradiated quartz.
6) The effect of the crack opening on the volume expansion became significant, as the neutron fluence increased. This crack behavior was considered important for concrete aging management in nuclear power plants.

Acknowledgments

This work was partially supported by the Japanese Concrete Aging Management Program on Irradiation Effects (JCAMP), funded by the Ministry of Economy, Trade, and Industry, Japan. The specimen was succeeded from the project “Advanced aging management technical evaluation of concrete structures in nuclear power plants,” funded by the Nuclear Regulation Authority (NRA, Japan). The work on the post-neutron irradiated samples, except for He-pycnometry and associated mass measurements, has been realized with the institutional support of the Ministry of Industry and Trade of the Czech Republic. He-pycnometry and associated mass measurements were sponsored by the US Department of Energy’s (DOE’s) Office of Nuclear Energy’s Light Water Reactor Sustainability program under contract DE-AC05-00OR22725 with UT Battelle LLC/Oak Ridge National Laboratory (ORNL) and by the US Department of Energy's (DOE's) Office of Nuclear Energy under the DOE Idaho Operations Office Contract DE-AC07-051D14517 as part of a Nuclear Science User Facilities experiment.

Conflicts of Interest

The authors declare no conflict of interest.

CRediT author statement

IM: Project administration, Conceptualization, Resources, Methodology, Funding acquisition, Software, Writing - Original Draft, Writing - Review & Editing

TK: Methodology, Investigation, Data Curation, Writing - Review & Editing

SS: Funding acquisition,Methodology, Investigation, Data Curation, Writing - Review & Editing

PH: Methodology, Investigation, Data Curation, Formal analysis

AF: Methodology, Investigation, Data Curation, Formal analysis

TO: Methodology, Writing - Review & Editing

KM: Methodology, Writing - Review & Editing

TI: Methodology, Formal analysis, Writing - Review & Editing

ET: Methodology, Investigation, Data Curation, Writing - Review & Editing

KS: Funding acquisition, Conceptualization, Project administration, Writing - Review & Editing

References

Bates, J. B., Hendricks, R. W. and Shatter, L. B., (1974). "Neutron irradiation effects and structure of noncrystalline SiO2." *The Journal of Chemical Physics*, *61*(10), 4163–4176.

Bolse, W., (1999). "Amorphization and recrystallization of covalent tetrahedral networks." *Nuclear Instruments and Methods in Physics Research, Section B: Beam Interactions with Materials and Atoms*, *148*(1–4), 83–92.

Brown, F. B., Barrett, R. F., Booth, T. E., Bull, J. S., Cox, L. J., Forster, R. A., Goorley, T. J., Mosteller, R. D., Post, S. E., Prael, R. E. and others, (2002). "MCNP version 5." *Trans. Am. Nucl. Soc*, *87*(273), 2–3935.

Bruck, P. M., Esselman, T. C., Elaidi, B. M., Wall, J. J. and Wong, E. L., (2019). "Structural assessment of radiation damage in light water power reactor concrete biological shield walls." *Nuclear Engineering and Design*, *350*(May), 9–20.

Bykov, V. N., Denisov, A. V, Dubrovskii, V. B., Korenevskii, V. V, Krivokoneva, G. K. and Muzalevskii, L. P., (1981). "Effect of irradiation temperature on the radiation expansion of quartz." *Soviet Atomic Energy*, *51*(3), 593–595.

Denisov, A., Dubrovskii, V. and Solovyov, V., (2012). "*Radiation resistance of mineral and polymer construction materials*." ZAO MEI Publishing House.

Doebelin, N. and Kleeberg, R., (2015). "Profex: a graphical user interface for the Rietveld refinement program BGMN." *Journal of Applied Crystallography*, *48*(5), 1573–1580.

Douillard, L. and Duraud, J. P., (1996). "Amorphization of α-quartz under irradiation." *Journal de Physique III*, *6*(12), 1677–1687. (被引用数:15Export Date: 16 April 2015)

Downs, R. T. and Hall-Wallace, M., (2003). "The American Mineralogist crystal structure database." *American Mineralogist*, *88*(1), 247–250.

Dubrovskii, V. B., Ibragimov, S. S., Ladygin, A. Y., Kulakovskii, M. Y. and Pergamenshchik, B. K., (1968). "Radiation stability of serpentine concrete." *Soviet Atomic Energy*, *25*(6), 1345–1346.

Dubrovskii, V. B., Ibragimo, S., Korenevs, V., Ladygin, A. Y., Pergamen, V. and Perevalo, V., (1970). "Hematite Concrete for Shielding Against High Neutron Fluxes." *Atomnaya Energiya (USSR)*, *28*(3), 258–260. (From Duplicate 1 (Hematite Concrete for Shielding against High Neutron Fluxes - Dubrovskii, V B; Ibragimo, Ss; Korenevs, Vv; Ladygin, A Y; Pergamen, Vk; Perevalo, Vs)H7332Times Cited:0Cited References Count:4)

Dubrovskii, V. B., Ibragimov, A., Ladygin, S. and Pergamenshckik, B. K., (1966a). "The effect of neutron irradiation on certain properties of refractory concretes." *Atomnaya Energiya*, *21*, 108–112.

Dubrovskii, V. B., Ibragimov, S. S., Ladygin, A. Y., Pergamenshchik, B. K. and Hodge, B., (1966b). "Radiation damage in ordinary concrete." *Atomnaya Energiya*, *23*(4), 310–316.

Elleuch, L. F., Dubois, F. and Rappeneau, J., (1972). "Effects of Neutron Radiation on Special Concretes and Their Components." *Special Publication*, *34*.

Field, K. G., Remec, I. and Pape, Y. Le, (2015). "Radiation effects in concrete for nuclear power plants - Part I: Quantification of radiation exposure and radiation effects." *Nuclear Engineering and Design*, *282*, 126–143.

Gates-Rector, S. and Blanton, T., (2019). "The powder diffraction file: a quality materials characterization database." *Powder Diffraction*, *34*(4), 352–360.

Giorla, A., Vaitová, M., Le Pape, Y. and Štemberk, P., (2015). "Meso-scale modeling of irradiated concrete in test reactor." *Nuclear Engineering and Design*, *295*(December), 59–73.

Gražulis, S., Chateigner, D., Downs, R. T., Yokochi, A. F. T., Quirós, M., Lutterotti, L., Manakova, E., Butkus, J., Moeck, P. and Le Bail, A., (2009). "Crystallography Open Database--an open-access collection of crystal structures." *Journal of Applied Crystallography*, *42*(4), 726–729.

Gupta, P. K., (1993). "Rigidity, Connectivity, and Glass-Forming Ability." *Journal of the American Ceramic Society*, *76*(5), 1088–1095.

Hilsdorf, H., Kropp, J. and Koch, H., (1978). "The effects of nuclear radiation on the mechanical properties of concrete." *ACI SP-55*, 223–251. (被引用数:10Export Date: 16 April 2015)

Hobbs, L. W., (1995). "The role of topology and geometry in the irradiation-induced

amorphization of network structures." *Journal of Non-Crystalline Solids*, *182*(1), 27–39.
Hsiao, Y. H., La Plante, E. C., Krishnan, N. M. A., Le Pape, Y., Neithalath, N., Bauchy, M. and Sant, G., (2017). "Effects of Irradiation on Albite's Chemical Durability." *Journal of Physical Chemistry A*, *121*(41), 7835–7845.
Ichikawa, Y., Maruyama, I., Wada, H., Yokokura, K., Ishikawa, S. and Saito, G., (2017). "Soundness evaluation method for concrete structures based on the data obtained from decommissioning Hamaoka nuclear power plant, Part 3: Investigation on core sampling method." *Proceeding of Annual Conf.of AIJ, Structure*, 1259–1260.
Johnson, F. B. and Pease, R. S., (1954). "The pile irradiation of quartz crystal oscillators." *Dublin Philosophical Magazine and Journal of Science*, *45*(365), 651–654.
Kambayashi, D., Sasano, H., Sawada, S., Suzuki, K. and Maruyama, I., (2020). "Numerical Analysis of a Concrete Biological Shielding Wall under Neutron Irradiation by 3D RBSM." *Journal of Advanced Concrete Technology*, *18*(10), 618–632.
Khmurovska, Y. and Štemberk, P., (2021a). "Catalogue of Radiation-Induced Damage of Rock Aggregates Identified by RBSM Analysis." *Journal of Advanced Concrete Technology*, *19*(6), 668–686.
Khmurovska, Y. and Štemberk, P., (2021b). "RBSM-based model for prediction of radiation-induced volumetric expansion of concrete aggregates." *Construction and Building Materials*, *294*, 123553.
Krishnan, N. M. A., Wang, B., Le Pape, Y., Sant, G. and Bauchy, M., (2017a). "Irradiation-vs. vitrification-induced disordering: The case of α -quartz and glassy silica." *Journal of Chemical Physics*, *146*(20), 204502.
Krishnan, N. M. A., Wang, B., Yu, Y., Le Pape, Y., Sant, G. and Bauchy, M., (2017b). "Enthalpy landscape dictates the irradiation-induced disordering of quartz." *Physical Review X*, *7*(3), 031019.
Li, Y., Le Pape, Y., Tajuelo Rodriguez, E., Torrence, C. E., Arregui Mena, J. D., Rosseel, T. M. and Sircar, M., (2020). "Microstructural characterization and assessment of mechanical properties of concrete based on combined elemental analysis techniques and Fast-Fourier transform-based simulations." *Construction and Building Materials*, *257*, 119500.
Luu, V. N., Murakami, K., Samouh, H., Maruyama, I., Suzuki, K., Prak Tom, P., Chen, L., Kano, S., Yang, H., Abe, H. and Suzuki, M., (2020). "Swelling of alpha-quartz induced by MeV ions irradiation: Critical dose and swelling mechanism." *Journal of Nuclear Materials*, *539*, 152266.
Martin, R. A., (1966). "*The effect of moisture on the compressive and tensile strength on a variety of rock materials*." University of Missouri at Rolla.
Maruyama, I., Takizawa, M., Sato, O., Etoh, J., Kontani, O., Sawada, S. and Ishikawa, S., (2017a). "Post-Japanese NRA Research Project On Soundness Evaluation Criteria For Radiation-Induced Concrete Degradation." In: IAEA Ed. *IAEA Fourth International Conference on Nuclear Power Plant Life Management*. Lyon, France: IAEA, CN246-70.
Maruyama, I., Kontani, O., Takizawa, M., Sawada, S., Ishikawa, S., Yasukouchi, J., Sato, O., Etoh, J. and Igari, T., (2017b). "Development of soundness assessment procedure for concrete members affected by neutron and gamma-ray irradiation." *Journal of Advanced Concrete Technology*, *15*(9), 440–523.
Mota, F., Caturla, M. J., Perlado, J. M., Dominguez, E. and Kubota, A., (2005). "Threshold energy of formation of an oxygen vacancy defect in SiO 2 by atomic displacements using molecular dynamics." *Fusion Engineering and Design*, *75–79*(SUPPL.), 1027–1030.
Murata, K. J. and Norman, M. B., (1976). "An index of crystallinity for quartz." *American Journal of Science*, *276*(9), 1120–1130.
Nakano, S., Muto, S. and Tanabe, T., (2005). "Change in Mechanical Properties of Ion-Irradiated Ceramics Studied by Nanoindentation Method." *Journal of the Japan Institute of Metals and Materials*, *69*(9), 815–824.
Ojo, O. and Brook, N., (1990). "The effect of moisture on some mechanical properties of rock." *Mining Science and Technology*, *10*(2), 145–156.
Okada, N., Ohkubo, T., Maruyama, I., Murakami, K. and Suzuki, K., (2020). "Characterization of irradiation-induced novel voids in *α* -quartz." *AIP Advances*, *10*(12),

125212.
Le Pape, Y., Field, K. G. and Remec, I., (2015). "Radiation effects in concrete for nuclear power plants, Part II: Perspective from micromechanical modeling." *Nuclear Engineering and Design*, *282*, 144–157.
Le Pape, Y., Sanahuja, J. and Alsaid, M. H. F., (2020). "Irradiation-induced damage in concrete-forming aggregates: revisiting literature data through micromechanics." *Materials and Structures/Materiaux et Constructions*, *53*(3), 1–35.
Le Pape, Y., Alsaid, M. H. F. and Giorla, A. B., (2018). "Rock-Forming Minerals Radiation-Induced Volumetric Expansion – Revisiting Literature Data." *Journal of Advanced Concrete Technology*, *16*(5), 191–209.
Le Pape, Y., Giorla, A. and Sanahuja, J., (2016). "Combined Effects of Temperature and Irradiation on Concrete Damage." *Journal of Advanced Concrete Technology*, *14*(3), 70–86.
Pomaro, B., (2016). "A Review on Radiation Damage in Concrete for Nuclear Facilities: From Experiments to Modeling." *Modelling and Simulation in Engineering*, *2016*.
Pomaro, B., Xotta, G., Salomoni, V. A. and Majorana, C. E., (2022). "A thermo-hydro-mechanical numerical model for plain irradiated concrete in nuclear shielding." *Materials and Structures/Materiaux et Constructions*, *55*(1), 1–28.
Primak, W., Fuchs, L. H. and Day, P., (1955). "Effects of Nuclear Reactor Exposure on Some Properties of Vitreous Silica and Quartz." *Journal of the American Ceramic Society*, *38*(4), 135–139.
Primak, W., (1958). "Fast-neutron-induced changes in quartz and vitreous silica." *Physical Review*, *110*(6), 1240–1254.
Saklani, N., Banwat, G., Spencer, B., Rajan, S., Sant, G. and Neithalath, N., (2021). "Damage development in neutron-irradiated concrete in a test reactor: Hygro-thermal and mechanical simulations." *Cement and Concrete Research*, *142*, 106349.
Sasano, H., Maruyama, I., Sawada, S., Ohkubo, T., Murakami, K. and Suzuki, K., (2020). "Meso-Scale Modelling of the Mechanical Properties of Concrete Affected by Radiation-Induced Aggregate Expansion." *Journal of Advanced Concrete Technology*, *18*(10), 648–677.
Silva, C. M., Rosseel, T. M. and Holliday, K. S., (2022). "Radiation-Induced Changes in Single Crystal Calcite and Dolomite: Mineral Analogues of Light Water Reactor, Nuclear Power Plant Concrete Aggregates." *Journal of Physical Chemistry C*, *126*(1), 634–646.
Silva, C. M., Rosseel, T. M. and Kirkegaard, M. C., (2018). "Radiation-Induced Changes in Quartz, A Mineral Analog of Nuclear Power Plant Concrete Aggregates." *Inorganic Chemistry*, *57*(6), 3329–3338.
Simon, I., (1957). "Structure of Neutron-Irradiated Quartz and Vitreous Silica." *Journal of the American Ceramic Society*, *40*(5), 150–153.
Torrence, C. E., Giorla, A. B., Li, Y., Rodriguez, E. T., Arregui Mena, J. D., Rosseel, T. M. and Le Pape, Y., (2021). "MOSAIC: An Effective FFT-based Numerical Method to Assess Aging Properties of Concrete." *Journal of Advanced Concrete Technology*, *19*(2), 149–167.
Wang, B., Yu, Y., Pignatelli, I., Sant, G. and Bauchy, M., (2015). "Nature of radiation-induced defects in quartz." *The Journal of Chemical Physics*, *143*(2), 024505.
Weber, W. J., Ewing, R. C. and Wang, L.-M., (1994). "The radiation-induced crystalline-to-amorphous transition in zircon." *Journal of Materials Research*, *9*(3), 688–698.
Wittels, M. C., (1957). "Structural behaviou of neutron irradiated quartz." *Philosophical Magazine*, *2*(24), 1445–1461.
Wittels, M. and Sherrill, F. A., (1954). "Radiation Damage in SiO2 Structures." *Physical Review*, *93*(5), 1117–1118. (PR) Retrieved from http://link.aps.org/doi/10.1103/PhysRev.93.1117.2
Wong, L. N. Y., Maruvanchery, V. and Liu, G., (2016). "Water effects on rock strength and stiffness degradation." *Acta Geotechnica*, *11*(4), 713–737.
Yuan, X., Pulim, V. and Hobbs, L. W., (2001). "Molecular dynamics refinement of topologically generated reconstructions of simulated irradiation cascades in silica networks." *Journal of Nuclear Materials*, *289*(1–2), 71–79.

884